Electron cyclotron resonance ion source plasma characterization by X-ray spectroscopy and X-ray imaging

David Mascali,[1,a)] Giuseppe Castro,[1] Sándor Biri,[2] Richárd Rácz,[2] József Pálinkás,[2] Claudia Caliri,[1,3] Luigi Celona,[1] Lorenzo Neri,[1] Francesco Paolo Romano,[1,4] Giuseppe Torrisi,[1,5] and Santo Gammino[1]
[1]*INFN–Laboratori Nazionali del Sud, Via S. Sofia 62, 95125 Catania, Italy*
[2]*Institute for Nuclear Research (Atomki), Hungarian Academy of Sciences, Bem tér 18/c, H-4026 Debrecen, Hungary*
[3]*Università degli Studi di Catania, Dip.to di Fisica e Astronomia, via Santa Sofia 64, 95123 Catania, Italy*
[4]*CNR, Istituto per i Beni Archeologici e Monumentali, Via Biblioteca 4, 95124 Catania, Italy*
[5]*Università Mediterranea di Reggio Calabria, DIIES, Via Graziella, I-89100 Reggio Calabria, Italy*

An experimental campaign aiming to investigate electron cyclotron resonance (ECR) plasma X-ray emission has been recently carried out at the ECRISs—Electron Cyclotron Resonance Ion Sources laboratory of Atomki based on a collaboration between the Debrecen and Catania ECR teams. In a first series, the X-ray spectroscopy was performed through silicon drift detectors and high purity germanium detectors, characterizing the volumetric plasma emission. The on-purpose developed collimation system was suitable for direct plasma density evaluation, performed "on-line" during beam extraction and charge state distribution characterization. A campaign for correlating the plasma density and temperature with the output charge states and the beam intensity for different pumping wave frequencies, different magnetic field profiles, and single-gas/gas-mixing configurations was carried out. The results reveal a surprisingly very good agreement between warm-electron density fluctuations, output beam currents, and the calculated electromagnetic modal density of the plasma chamber. A charge-coupled device camera coupled to a small pin-hole allowing X-ray imaging was installed and numerous X-ray photos were taken in order to study the peculiarities of the ECRIS plasma structure.

I. INTRODUCTION

The inside of an Electron Cyclotron Resonance Ion Source (ECRIS) plasma, made of multicharged ions immersed in a dense cloud of energetic electrons, is confined by multi-Tesla magnetic fields and resonantly heated by microwaves in the 2.45-28 GHz frequency range. While until 2004-2005 the output currents and charge states were deemed to depend only on a global scaling of macroscopic plasma parameters (density and temperature), more recently plasma instabilities,[1] local fluctuations and/or non-uniform distribution of the plasma density,[2] non-linear response of the electron heating to the pumping wave frequency, or sensitivity to slight adjustments of the magnetic field have been correlated with the intensity and emittance of the plasma-generated beams.[3] All these "signs" demonstrate the wave-to-plasma interaction in a closed resonant cavity (i.e., the ECRIS plasma chamber) with small size-to-waveguide ratio is still not fully exploited. A limiting factor in the complete understanding of the above mentioned issues exists as due to the few types of diagnostics tools so far designed and installed especially because of the compactness of these machines. Any significant step forward in ECRIS physics and technology will require diagnostic tools of various types, from microwave interferometry to X-ray spectroscopy, including high resolution X-ray spectroscopy and spatially-resolved X-ray spectroscopy made by quasi-optical methods (as pin-hole cameras, see, for example, pioneering experiments in Atomki–Debrecen already in 2002-2003[4,5]). The present work shows a characterisation of the Atomki-ECRIS plasma under different conditions of heating (tuning of the frequency and magnetic field especially), performed by a wide gamma of detectors sensitive in different ranges of the X-ray spectrum. The results give a deep insight into the ECRIS physics; they are, in perspective, very useful also for a direct comparison with the numerical modelling that is now ongoing, and whose result publication is postponed for another paper.

The outputs of the Gesellschaft für Schwerionenforschung, (Darmstadt, Germany) experiment performed during 2013[6] showed that the frequency impact on the plasma heating could be relevant (especially in the buildup of the warm electron population) as a consequence of the wave-to-plasma coupling mediated by the resonator nature of the plasma chamber. The following idea was that space resolved X-ray measurements would be necessary in order to investigate how the plasma structure in the "warm electrons" domain was eventually affected by resonant modes. That experiment

Note: Contributed paper, published as part of the Proceedings of the 16th International Conference on Ion Sources, New York, New York, USA, August 2015.
[a)]davidmascali@lns.infn.it

was affected by a limiting—even though unavoidable on that setup—drawback, existing in the "two-stage" measurement method of X-ray emission and CSD (charge state distribution) recording. It did not allow to record contemporaneously the ion output currents and plasma emitted X-rays. An upgraded setup, overcoming this limitation, has been arranged on the Atomki-Debrecen ECRIS,[7] allowing to perform plasma X-ray measurements in the high energy (>30 keV) and medium energy (2-30 keV) domains, with the contemporaneous extraction of the ion beam and the 2D imaging of the plasma through an X-ray pin-hole camera method.

II. EXPERIMENTAL SETUP

The new setup is based on SDD—Silicon Drift Detectors and HpGe—High Purity Germanium detectors that were used to formerly characterize the volumetric plasma emission, and then on a Charge-Coupled Device (CCD) camera coupled to a small pin-hole for 2D X-ray imaging and 2D-resolved spectroscopy. The experiment was performed in November 2014 at Atomki–Debrecen (Hungary). In order to provide the above-mentioned direct relationship between the CSD and the plasma spectrum, the SDD and CCD detectors were placed on the injection side of the Atomki-ECRIS, according to the setup displayed by Figure 1.

Figure 1 shows how the different detectors were placed in order to make possible contemporaneous measurements of X-rays and CSD. The SDD was placed beyond a 8 μm kapton foil for vacuum break and collimated by a lead cylinder with a drilled hole of ϕ = 1 mm and 155 mm in length. The HpGe detector was used for monitoring the X-rays generated by the high energy electrons—from inside the plasma or when impinging on the chamber walls. The detector was collimated by lead blocks of 2 cm in thickness, ϕ = 1 mm, and then placed beyond the bending magnet, after a quartz window of 1 cm in thickness. The HpGe detected the radiation passing mostly through the extraction hole of the plasma chamber. The source was optimized for producing Ar4+ ions, with coils energized at 100% able to guarantee ECR condition

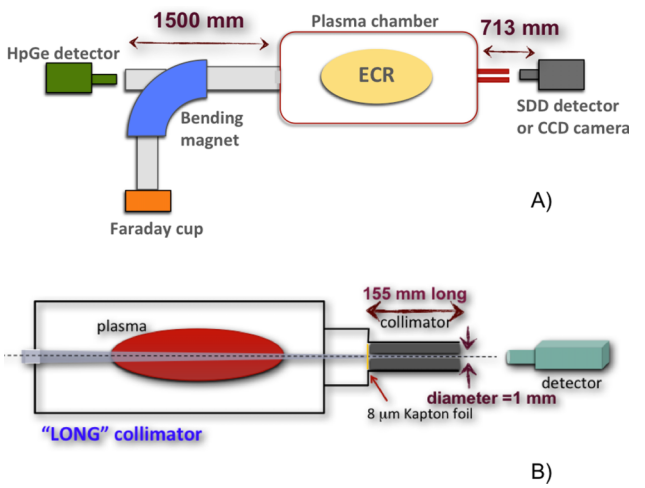

FIG. 1. Sketch of the experimental setup: (a) general layout including distances at which detectors were placed; and (b) collimation strategy in order to filter out X-rays from the walls.

around 13 GHz. The RF power injected to the plasma chamber was kept fixed at 30 W in order to avoid the effect of the different power absorption in the microwave transmission system (waveguides, bands, twists, etc.) as a function of the RF frequency. The injected power was measured at the closest possible point (at a distance of 130 cm from the plasma chamber entrance) by using directional coupler. The length of the total waveguide system (from amplifier output to the plasma chamber input) was 180 cm. The low power level was preferred in order to prevent high dead-times in the SDD detector and pixel-saturation in the CCD camera. In the first part of the experimental campaign, we only made use of SDD and HpGe setups, in order to define the operative conditions including the set of frequencies for exploring the "frequency tuning effect" (FTE). The SDD "long collimator" configuration was calculated in order to avoid any interception of the cone of view with the extraction endplate (the cone lies exactly within the extraction hole). In this way, the detected X-rays can be considered as solely emitted by the plasma bulk itself, allowing plasma density and temperature calculation along the line of sight. After the SDD measurements, the CCD made by 256 × 1024 pixels and with an optimal quantum efficiency in the range 500 eV–10 keV, approximately was coupled to a lead pin-hole and placed along the axis, facing the chamber from the injection flange (see Figure 1 (a)). The plasma chamber inspection was allowed by a metallic mesh covering about the 60% of the injection endplate. In addition, aluminum windows of variable thicknesses (range 1–6 μm) were used to screen the CCD from the visible and UV light coming out from the plasma. Additional and more precise details concerning the measurements setups can be found in another paper.[8]

III. EXPERIMENTAL RESULTS

ECRIS plasmas display non-isotropic electron energy distribution function (EEDF) due to cyclotron acceleration and magnetic confinement, reflecting on anisotropic X-ray emission. According to non-isotropic models[9,10] fitting experimentally measured data, the relative error one makes assuming isotropic EEDF—with respect to anisotropic cases—is around 10%-15% when considering electron temperatures below 25-30 keV; the error grows with growing temperatures. Considering the low RF power level used for the present work (<40 W), we expect to obtain warm electron temperatures below the mentioned threshold and we deemed that it was convenient to use simplified, fully isotropic models for X-ray spectra fitting, like the one coming from Gumberidze *et al.* paper.[11]

In this context, the plasma emitted spectrum is re-elaborated in order to define the so-called "spectral emissivity curve" providing the total equivalent number of photons emitted in the given energy interval over the entire sold angle, defined as $N^P(h\nu)$,

$$J(h\nu) = h\nu \frac{N^p(h\nu)}{t} \frac{4\pi}{\Delta E V_p \Omega_{Tot}} = h\nu \frac{N^{ch}(h\nu)}{\varepsilon_g t} \frac{4\pi}{\Delta E V_p \Omega_{Tot}}, \quad (1)$$

where $N^{ch}(h\nu)/\varepsilon_g = N^P(h\nu)$, V_p is the plasma volume, Ω_{Tot} the entire solid angle, t is the acquisition time, and ΔE is

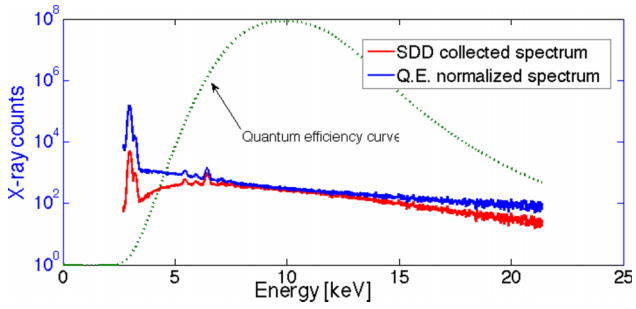

FIG. 2. Raw and renormalized spectra collected by the SDD detector in "lead-long-collimator" configuration.

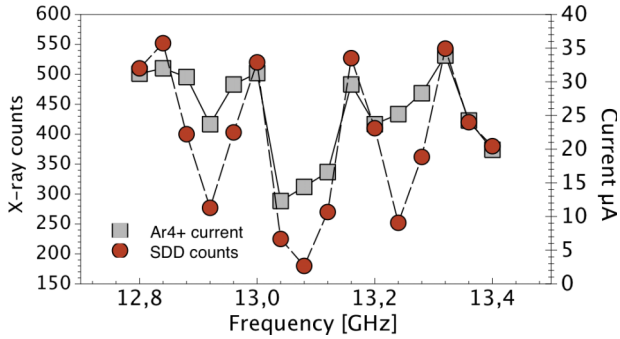

FIG. 3. Trend of Ar4+ extracted current as compared with the total counts detected by the SDD detector.

the energy per channel. Similar to what was done in previous measurements,[6] the renormalization of the total number of emitted photons was done by a Monte-Carlo code, allowing to determine the geometrical efficiency of the SDD detector when placed beyond the long lead collimator (Fig. 1). The emissivity is then fitted by the curve

$$J_{M\text{-}K}(h\nu) = N_i N_e (Z\hbar)^2 \left(\frac{4\alpha}{\sqrt{6m_e}}\right)^3 \left(\frac{\pi}{kT_{Mw}}\right)^{1/2} e^{(-h\nu/kT_{Mw})}, \quad (2)$$

thus determining N_i and N_e and electron temperature, T_M.

Figure 2 shows a representative spectrum of X-rays emitted by the plasma when the quantum efficiency of the SDD detector has been calculated and applied on the raw data. The Ar K_α and K_β peaks (around 3 keVs) are evident; the very good collimation system allowed to reduce the Fe and Cr peaks, now due to some residual scattering coming out from the stainless-steel mesh placed at the injection end-plate. The numerically estimated geometrical efficiency was equal to 1.16×10^{-6}.

A sequence of frequencies—with a constant step of 40 MHz, from 12.80 to 13.40 GHz—was selected in order to explore the X-ray emission in the low- and high-energy ranges, recording the CCD images, the output currents of Ar4+, and the complete CSD at the same time.

According to the results shown in Fig. 3 and Table I, there is an almost-exact correlation between the rate (counts/s) detected by SDD and the recorded Ar4+ current: Figure 3 highlights wide fluctuations in both the recorded data (of a factor 2.5 as concern X-ray flux, of a factor 3.5 regarding the Ar4+ current). Three frequencies were then selected (as highlighted in Table I) in order to perform CCD measurements retrieving X-ray transversal imaging that will be shown later-on. The 12.84 and 12.92 GHz frequencies were selected as being the two frequencies producing the broadest fluctuation in both X-ray flux and output current, while 13.24 GHz represents a significant frequency since the increase of output current does not correspond—as occurs for the other data—to a comparable increase of X-ray flux.

The collection of results elaborated after the experimental campaign is illustrated in the sequence of Figures 4(a)-4(f). Figure 4(a) shows the trend of the average charge state $\langle q \rangle$ as a function of the frequency. In a similar way to the Ar4+ current, the $\langle q \rangle$ also fluctuates widely when tuning the frequency.

The trend is almost exactly similar to the plasma response in terms of density and temperature, as it can be seen in Figures 4(b) and 4(c). The spectral temperature fluctuates from 16 to 22 keV, while the density lies in the range 2.5–5.5 10^{16} m^{-3}. The experimental error in both cases was within 10%. Figure 4(d) illustrates the trend of $\langle q \rangle$ with respect to the plasma energy content, calculated as $n_e T_e$ from the aforementioned density and temperature values obtained by the SDD detector. Each point corresponds to a different frequency: $\langle q \rangle$ clearly grows with the energy content, but the scattered points demonstrate that for some conditions it is however not strictly a matter of density or temperature (or the product between them); sometimes, different $\langle q \rangle$ are obtainable by different combinations of energy contents, depending on the pumping wave frequency. In order to investigate the quasi-regular fluctuation of density and temperature with respect to the RF frequency, we computed the electromagnetic modes of the Atomki-ECRIS plasma chamber, assuming, at the beginning, a fully closed chamber of stainless steel without plasma inside. The results are shown in Figure 4(e) and illustrated as the trend of the modal density (i.e., the histogram of the number of modes vs. the frequency) that can be excited in the plasma chamber when changing the frequency. Except a slight

TABLE I. Summary of the frequency set, including SDD counts, dead time, and Ar-4+ currents.

f (GHz)	Ar4+ (μA)	SDD (counts/s)	Dead time (%)	I_T (mA)
12,8	32	16 639	6,4	1,03
12,84	**33,7**	**19 844**	**7**	**1,02**
12,88	30	14 766	5,6	0,94
12,92	**25**	**9 557**	**4**	**0,89**
12,96	31,2	14 233	5,5	0,98
13	31,7	19 619	7	1
13,04	22	8 973	3,7	0,86
13,08	13,2	6 490	2,5	0,76
13,12	17,8	10 017	3,9	0,84
13,16	32,7	20 148	7	0,96
13,2	25,9	14 909	5,4	0,94
13,24	**26,8**	**8 813**	**3,3**	**0,9**
13,28	28,5	12 989	4,8	0,91
13,32	32,5	19 779	6,8	0,99
13,36	28,1	14 465	5,3	0,95
13,4	25,8	13 740	4,9	0,93

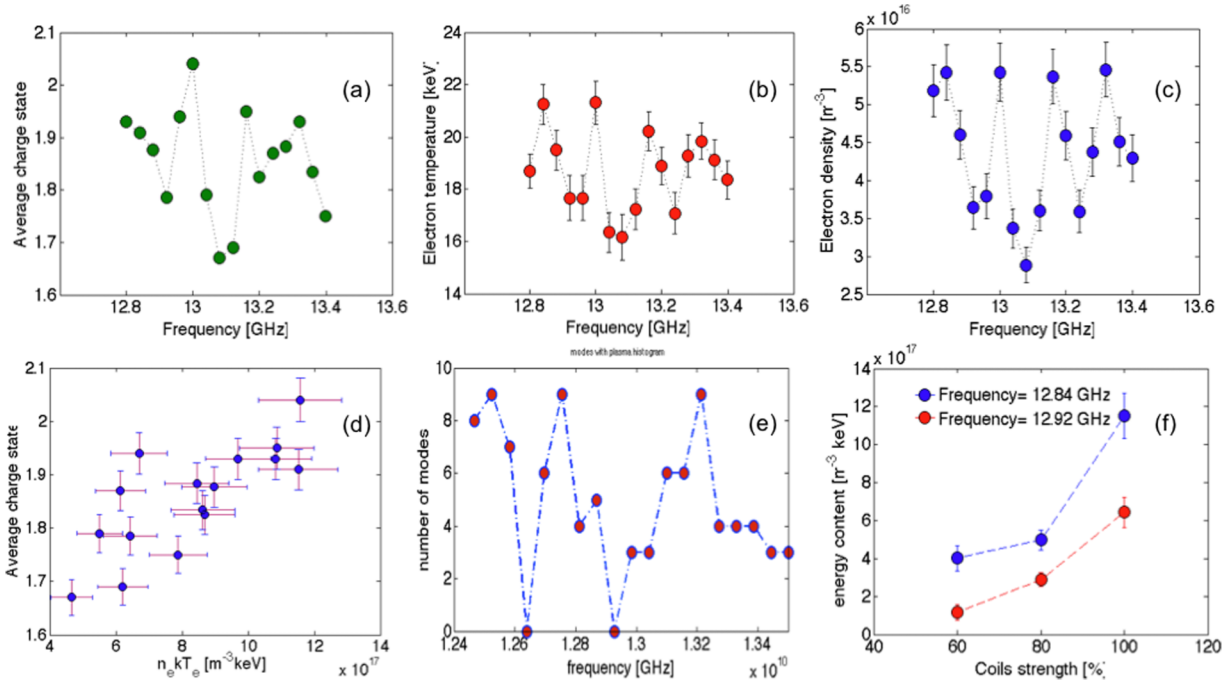

FIG. 4. From up-left, clockwise direction: (a) trend of the average charge state vs. the pumping wave frequency; (b) trend of the electron temperature in the 2-30 keV energy domain vs. the pumping wave frequency; (c) trend of the electron density (m^{-3}) in the 2-30 keV energy domain vs. the pumping wave frequency; (d) trend of the average charge state vs. the plasma energy content $n_e T_e$; (e) electromagnetic modal density as calculated by COMSOL for the Atomki-ECRIS plasma chamber; and (f) response of the plasma energy content (m^{-3}keV) axial confinement coils strength, for two different operative frequencies.

shift (due to "empty-chamber" calculations, while the plasma upshifts the modes because of its electrical permittivity), the modal density trend nicely reproduces the fluctuating trends of $\langle q \rangle$, n_e and T_e, displaying a similar number of "peaks" and "valleys" in a comparable frequency range.

Therefore, we explored the trend of the output currents for the selected charge state when changing the coil strength, as shown in Figure 4(f), for two different frequencies. Data show that the energy content of the plasma grows non-linearly with the current flowing in the coils, and the growth depends strongly on the pumping wave frequency, thus displaying a strong interplay between frequency and magnetic field. The analysis of HpGe detector collected spectra found the same fluctuations as SDD, but with a decreasing trend in terms of both total counts and spectral temperature, probably due to the decreasing power density deposited into the plasmoid at increasing frequencies (B_{ECR}/B_{min} increases) or due to different fluxes of escaping electrons in axial/radial directions.

The experiment continued by using the CCD for an inspection of "space-resolved" emitted X-ray from the plasma chamber (i.e., including the radiation emitted from the plasma and from the plasma chamber walls). Figure 5 shows a direct comparison between (a) the plasma as it is seen by naked eye and (b) the plasma as it can be seen by the X-ray camera; Fig. 5(c) shows a photo of the plasma electrode with the extraction hole in it. The sequence of Figures 6(a)-6(f) illustrates the obtained X-ray images for the three frequencies mentioned above. Each picture can be roughly subdivided into three different regions of interest (ROIs): the ROI-1, i.e., near axis zone (denominated "hole" region, corresponding to the extraction hole); the ROI-2, i.e., the so-called "plasma region"; the ROI-3, i.e., the "magnetic pole" region. All the X-ray photos are spectrally integrated; therefore, taking differentiation between the X-ray photons affected by the plasma electrons or by the lost electrons is possible only in the regions where they can be separated geometrically (not spectrally), e.g., in the cases of ROI-1 and ROI-3. ROI-1 counts not all but just those photons produced by the plasma electrons since there is no overlapping area "behind" the plasma from where wall bremsstrahlung appears. While ROI-3 counts not all but just those photons that are produced by the escaping electrons to the lateral wall of the plasma chamber, since the coordinates of those spots are corresponding to the superficies of the plasma chamber. From a general inspection of the pictures, it is clearly visible that other than the hole in the near axis region, there are branches due to the electrons escaping from the confinement. The ratio between ROI-1 and ROI-2 emissivity depends on the frequency, as it can be clearly seen. It is also evident how strong is the frequency impact on the overall emissivity of the plasma, even of one order of magnitude when going from 12.84 to 12.92 GHz. The lower row of pictures moreover highlights the response of

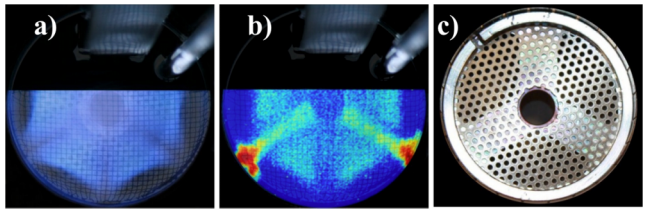

FIG. 5. Views of the plasma chamber from the position of the X-ray camera: (a) plasma as seen by our naked eye, (b) plasma as seen by the X-ray camera, and (c) photo of the plasma electrode.

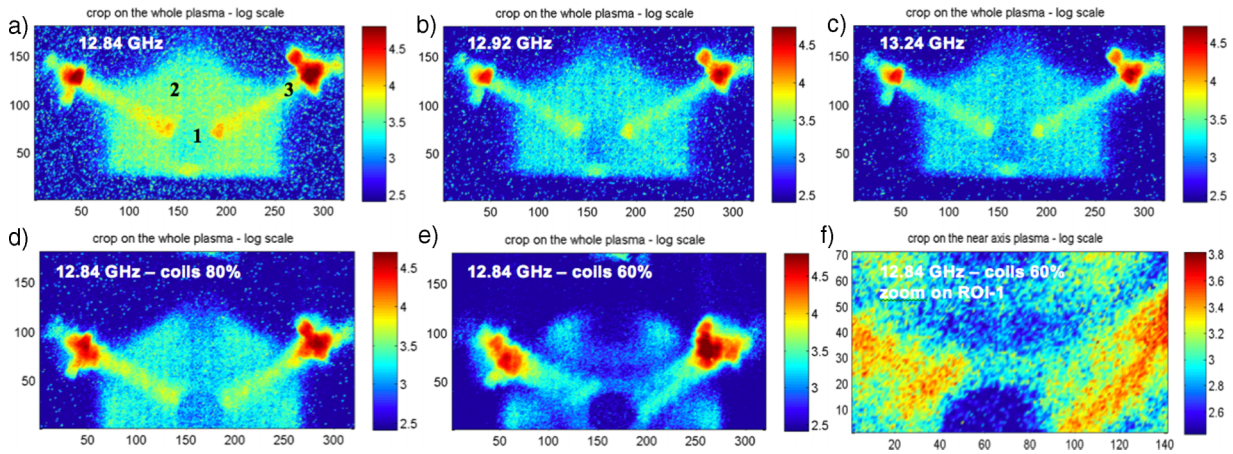

FIG. 6. From up-left, clockwise direction: (a) 2D-imaging of the plasma at 12.84 GHz; (b) 2D-imaging of the plasma at 12.92 GHz; (c) 2D-imaging of the plasma at 13.24 GHz; (d) 2D-imaging of the plasma at 12.84 GHz, coils at 80% of the maximum strength; (e) 2D-imaging of the plasma at 12.84 GHz, coils at 60% of the maximum strength; and (f) zoom around the plasma chamber axis, the same as configuration. The colour scale is given in 10^{x}, x being the numbers labelling the colourbar.

the plasma structure to the tuning of the magnetic field. Once the frequency is fixed at 12.84 GHz, we decreased the coils' strength by 20% (Figure 6(d)), then by 40% (Figure 6(e)). It was evident that the decrease of the plasma density in the near axis region (very clear when looking to Figure 6(f) that is a zoomed image in the near axis region), corresponding to a strong growth of the emission at the magnetic pole, that is a clear sign of enhanced electrons deconfinement. In addition to the general decrease of the plasma energy content and X-ray emissivity—as confirmed by Figure 6(f)—the plasma starts to accumulate in well-defined localized regions. A more detailed analysis of the CCD pictures is far beyond the content and allowed length of this paper. A full summary and interpretation of the pinhole camera results together with a comparison between experimental results and model calculations will be published in a separate paper.

IV. CONCLUSION

A systematic experimental study of the plasma emitting X-ray radiation was carried out at the Atomki-ECR ion source. The direct main goal was to investigate the effect of the microwave frequency to the plasma and to the microwave-plasma interaction. Three X-ray detectors were applied (always two of them, simultaneously) together with on-line beam extraction. SDD results revealed strong correlation between plasma and beam parameters (plasma parameters: X-ray counts, electron temperature, and density; beam parameters: analysed beam intensity and average charge). CCD images show significant differences of the energy content and displacement of the plasma vs. microwave frequency.

ACKNOWLEDGMENTS

The research leading to these results has received funding from the European Union Seventh Framework Program FP7/2007-2013 under Grant Agreement No. 262010–ENSAR. The EC is not liable for any use that can be made on the information contained herein. Additional funds were supported by INFN—5th Nat. Comm. under the RDH experiment.

[1]O. Tarvainen, I. Izotov, D. Mansfeld, V. Skalyga, S. Golubev, T. Kalvas, H. Koivisto, J. Komppula, R. Kronholm, J. Laulainen, and V. Toivanen, Plasma Sources Sci. Technol. **23**, 025020 (2014).
[2]D. Mascali, G. Torrisi, L. Neri, G. Sorbello, G. Castro, L. Celona, and S. Gammino, Eur. Phys. J. D **69**, 27 (2015).
[3]L. Celona, G. Ciavola, F. Consoli, S. Gammino, F. Maimone, P. Spaedtke, K. Tinschert, R. Lang, J. Mader, J. Rosbach, S. Barbarino, R. S. Catalano, and D. Mascali, Rev. Sci. Instrum. **79**, 023305 (2008).
[4]S. Biri, A. Valek, T. Suta, E. Takács, Cs. Szabó, L. T. Hudson, B. Radics, J. Imrek, B. Juhász, and J. Pálinkás, Rev. Sci. Instrum. **75**, 1420 (2004).
[5]E. Takács, B. Radics, C. I. Szabó, S. Biri, L. T. Hudson, J. Imrek, B. Juhász, T. Suta, A. Valek, and J. Pálinkás, Nucl. Instrum. Methods Phys. Res., Sect. B **235**, 120 (2005).
[6]D. Mascali, L. Celona, F. Maimone, J. Maeder, G. Castro, F. P. Romano, A. Musumarra, C. Altana, C. Caliri, G. Torrisi, L. Neri, S. Gammino, K. Tinschert, K. P. Spaedtke, J. Rossbach, R. Lang, and G. Ciavola, Rev. Sci. Instrum. **85**, 02A956 (2014).
[7]S. Biri, R. Rácz, and J. Pálinkás, Rev. Sci. Instrum. **83**, 02A341 (2012).
[8]R. Rácz, S. Biri, J. Pálinkás, D. Mascali, G. Castro, C. Caliri, F. P. Romano, and S. Gammino, Rev. Sci. Instrum. **87**, 02A741 (2016).
[9]C. Barué, M. Lamoureux, P. Briand, A. Girard, and G. Melin, J. Appl. Phys. **76**, 2662 (1994).
[10]Y. Higurashi, J. Ohnishi, T. Nakagawa, H. Haba, M. Tamura, T. Aihara, M. Fujimaki, M. Komiyama, A. Uchiyama, and O. Kamigaito, Rev. Sci. Instrum. **83**, 02A308 (2012).
[11]A. Gumberidze, M. Trassinelli, N. Adrouche, C. I. Szabo, P. Indelicato, F. Haranger, J.-M. Isac, E. Lamour, E.-O. Le Bigot, J. Mérot, C. Prigent, J.-P. Rozet, and D. Vernhet, Rev. Sci. Instrum. **81**, 033303 (2010).